



Testing, numerical analysis and design of CFDST cross-sections with square stainless steel outer tubes in bending

Fangying Wang^{a,*}, Ben Young^b, Leroy Gardner^c

^a Department of Civil Engineering, University of Nottingham, Nottingham, UK

^b Department of Civil and Environmental Engineering, The Hong Kong Polytechnic University, Hong Kong, China

^c Department of Civil and Environmental Engineering, Imperial College London, London, UK

ARTICLE INFO

Keywords:

CFDST
Experiments
Four-point bending tests
Moment capacities
Numerical modelling
Stainless steel

ABSTRACT

The structural performance and design of concrete-filled double skin tubular (CFDST) cross-sections with square stainless steel outer tubes are studied herein. A total of 17 four-point bending tests on CFDST cross-sections with varying concrete grades, together with accompanying material tests, were first conducted. The details of the test rig and procedures, as well as the key experimental results are reported. Following the physical testing, a numerical modelling campaign was carried out. A finite element (FE) model was initially validated against the tests, and then adopted to conduct a parametric study to acquire further FE data, covering a broader spectrum of material strengths and cross-section slendernesses. The obtained test and FE results were used to evaluate the applicability of the general design provisions for concrete-filled carbon steel members in the current European and American design codes. Overall, the examined design codes are shown to provide unduly conservative (less so for the higher concrete grades) and rather scattered moment resistance predictions, though some moment resistances predicted using the European code were on the unsafe side. Modifications to the European design treatment in relation to the assumed stress distribution, to take due account of the partial spread of plasticity in the outer tube, and the effective compressive strength of the concrete infill, to reflect the reduced relative effectiveness of using higher concrete grades, are proposed and shown to improve the consistency of the resistance predictions.

1. Introduction

Concrete-filled steel tubular (CFST) sections have been shown to offer excellent structural efficiency and constructability for use in a range of heavy structural applications, such as columns in high rise buildings, as well as piers and arches in bridges [1–4]. The improved structural efficiency is attributed principally to the composite action between the steel tube and the concrete infill, in particular, the reduced susceptibility to local buckling of the outer tube owing to the presence of the concrete infill inhibiting inward deformations, as well as the increased strength and ductility of the concrete infill due to the confinement offered by the outer tube [5]. CFST members also provide improved constructability associated with the outer tube acting as permanent formwork for the concrete infill. Considering the insignificant contribution of the central core area of concrete infill to the overall flexural stiffness, an alternative cross-section type, featuring a hollow steel tube to replace the inner concrete core, i.e. concrete-filled double

skin tubular (CFDST) cross-sections, has recently been put forward, and applied as columns in a transmission tower [6] and wind turbine [7]. The idea of using double skin tubular sections originated in Britain, where double cylindrical shells filled with resin were used in deep-water vessels to prevent instability under external pressure [8]. In the late 1990s, considering the favourable attributes derived from the use of a hollow inner tube associated with reduced weight and enhanced stiffness, potential applications of CFDST members in offshore structures [9] and bridge piers [10] were explored. From 2000 onwards, substantial research efforts have been devoted to examining the structural performance of CFDST cross-sections and members [11]. CFDST cross-sectional configurations are diverse, with various combinations of outer and inner tubular profiles to suit different structural applications. CFDST cross-sections with circular hollow section (CHS) outer tubes have been seen in most applications [11], owing to the strong confinement afforded to the concrete infill, thereby exploiting composite action to the greatest extent [12]. CFDST cross-sections with square or

* Corresponding author.

E-mail address: fangying.wang@nottingham.ac.uk (F. Wang).

<https://doi.org/10.1016/j.jcsr.2023.108125>

Received 9 January 2023; Received in revised form 19 June 2023; Accepted 13 July 2023

Available online 1 August 2023

0143-974X/© 2023 The Authors. Published by Elsevier Ltd. This is an open access article under the CC BY-NC-ND license (<http://creativecommons.org/licenses/by-nc-nd/4.0/>).

rectangular hollow section (SHS/RHS) outer tubes have also been considered in construction for their high bending stiffnesses and the relative ease of forming connections [13]. CFDST cross-sections with SHS outer and CHS inner profiles (see Fig. 1) in bending are the focus of the present study.

An increasing emphasis on sustainability, resilience and life-cycle considerations has prompted greater use of stainless steels as alternatives to carbon steels in the construction sector [14]. Use of stainless steel for the outer tubes of CFDST cross-sections has been recently proposed [15] to exploit the combined advantages of high ductility and durability that characterise stainless steel with the composite action seen in CFDST members. This combination of properties makes this section type potentially suitable for applications in aggressive and demanding environments, such as in the nuclear industry, marine and offshore engineering sectors, and in earthquake-prone zones.

In practical applications to date, CFDST cross-sections have generally been used for compression members [1,11]. This has been echoed in research, where the focus of research interest has been the compressive response of CFDST members with stainless steel outer tubes. Specifically, Han et al. [15] carried out a series of tests on straight, tapered and inclined stub columns, and concluded that the inclination and tapering both had a moderate negative influence on load-carrying capacity. Hassanein et al. [16] conducted a numerical investigation into circular CFDST stub columns with lean duplex stainless steel outer tubes and proposed design rules with modified coefficients accounting for the strain hardening of stainless steel materials. The authors [12,17–19] explored the structural behaviour and design of CFDST stub columns with austenitic, lean duplex and ferritic stainless steel outer tubes, and proposed modifications to current design rules incorporating a higher buckling coefficient to consider outward only local buckling in the outer tube and a reduction factor for high concrete grades. Wang et al. [20] carried out a comparative numerical study of CFDST stub columns with stainless steel and carbon steel outer tubes, and revealed that CFDST stub columns with stainless steel outer tubes exhibited high ductility and enhanced axial capacity over equivalent sections with carbon steel outer tubes attributed to substantial strain-hardening of the stainless steel material. Zheng et al. [21] conducted an experimental and numerical investigation of CFDST long columns under constant axial compressive load and lateral cyclic loading and compared the behaviour of CFDST members and equivalent members with fully filled inner tubes. Zhao et al. [22] examined the behaviour and design of CFDST long columns through the axial compressive testing of 12 specimens, and followed by FE modelling. One of the notable conclusions drawn from these investigations into CFDST members under compression is that the slenderness and strain hardening characteristics of stainless steel [23] have a

strong influence on the ultimate capacity and ductility of the CFDST members.

Structural members are often subjected to a combination of axial compression and bending, with flexure arising, for example, from inevitable eccentricities of axial loads, frame action, second order effects and transverse loads (e.g. wind and seismic loadings) [24]. This requires the member to be designed as a beam-column using moment-axial ($M-N$) interaction curves, for which the column buckling resistances and cross-sectional bending resistances serve as the end anchor points. Therefore, it is of fundamental importance to advance the understanding of the behaviour and resistance of CFDST cross-sections in pure bending, and this has been the subject of a number of recent research investigations. Previous experimental investigations have addressed carbon steel CFDST beams comprising circular [25–28], square [26,29], rectangular [30] or dodecagonal [31] hollow sections for both the outer and inner tubes, while carbon steel CFDST beams with different outer and inner profiles were examined in [32]. Finite element (FE) modelling has also been employed to investigate the structural response of CFDST beams [22,27,28,31]. It was found in these studies that CFDST beams exhibit high ductility and enhanced moment capacity, beyond the sum of the individual parts, due to the development of composite action between the steel tubes and concrete infill, and current design provisions for composite structures were found to be rather conservative. The flexural response of CFST beams with stainless steel outer tubes has also been recently explored by other researchers [33–38]; the significant influence of the slenderness of the stainless steel tube on the moment capacity and ductility was highlighted in these studies. A preliminary experimental investigation was carried out by Yang and Ma [33], where normal concrete and recycled aggregate concrete were employed as the infill material. Further work on lean duplex stainless steel CFST beams filled with different grades of concrete (C40–C110) was described by Deng and Young [34], where the effect of concrete strength on the overall moment capacity was found to be insignificant. This observation was also mirrored in the work of Chen et al. [35,36], where experiments were carried out on CFST beams with circular, square and rectangular austenitic stainless steel outer tubes. More recently, Gunawardena and Aslani [37,38] reported experimental and numerical investigations into CFST beams with spiral-welded stainless steel tubes; a decreasing level of conservatism in moment capacity predictions with increasing section slenderness was generally observed in these studies. To date, investigations into CFDST beams employing stainless steel outer tubes have been rather scarce, with a few tests reported on CFDST cross-sections with CHS outer tubes in bending [22,39]. Further research is thus required to fully address the flexural behaviour of CFDST cross-sections with stainless steel outer tubes and to devise safe, efficient and reliable design provisions to facilitate their broader adoption in practice.

As part of a wider research programme initiated by the authors to explore the structural behaviour and design of CFDST members with stainless steel outer tubes [12,17–19,39], the present study examines CFDST cross-sections with stainless steel SHS outer tubes and high strength steel CHS inner tubes in bending experimentally and numerically. In the experimental programme, five CFDST cross-section profiles with varying concrete grades were examined in a four-point bending configuration; accompanying material tests were also carried out. Following this, FE models were developed to reproduce the test observations and then used to perform a parametric study considering a range of material strengths and cross-section slendernesses. The combined set of test and FE results is compared with the moment resistance predictions calculated using the general design provisions for concrete-filled carbon steel members given in EN 1994-1-1 [40] and AISI 360–16 [41], enabling the applicability of these design provisions to the studied CFDST cross-sections to be evaluated. Finally, modifications to the current design rules are proposed and assessed through comparisons with the data generated in this study.

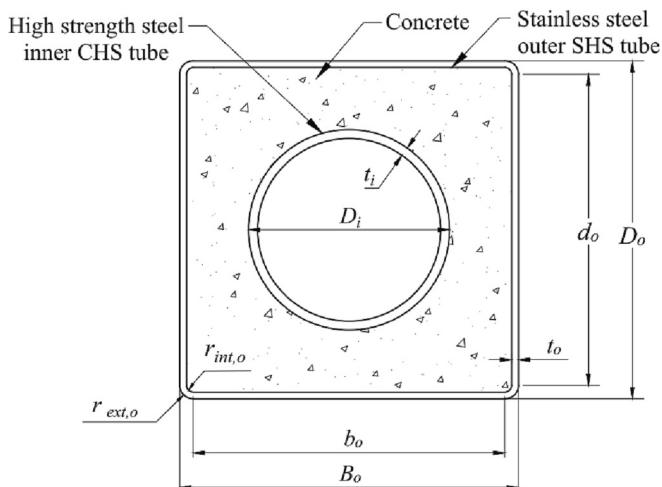


Fig. 1. Typical square CFDST cross-section.

2. Test programme

2.1. Overview

A comprehensive physical testing programme on the flexural response of CFDST beams with stainless steel SHS outer tubes and high strength steel CHS inner tubes is described. Five CFDST cross-sections were examined, employing Grade EN 1.4062 austenitic stainless steel SHS $120 \times 120 \times 6$ (depth \times width \times thickness in mm) and SHS $150 \times 150 \times 3$ as the outer profiles, and high strength steel hot-rolled CHS 22×4 (diameter \times thickness in mm) and CHS 32×6 as well as cold-formed CHS 89×4 as the inner profiles. For each cross-section, three grades of sandwiched concrete—C40, C80 and C120—with corresponding nominal concrete cylinder compressive strengths of 40, 80 and 120 MPa,

were employed. A total of 15 CFDST beam specimens with two repeats were prepared; the list of the specimens is shown in Table 1. The identification system of the specimens was designed to identify the CFDST cross-section constituents directly, beginning with the letter “B” indicating a beam specimen, followed by three identifiers corresponding to the outer tube, inner tube and concrete infill. For example, B-AS150 \times 3-HC89 \times 4-C120 defines a CFDST beam specimen with an AS150 \times 3 outer tube, in which the letter “A” stands for austenitic stainless steel and “S” signifies an SHS, and an HC89 \times 4 inner tube, with “H” referring to high strength steel and “C” indicating a CHS. The last term denotes concrete infill with a nominal cylinder compressive strength of 120 MPa. A letter ‘R’ is used for the repeat test. Geometric measurements were taken on the steel tubes prior to concrete casting, including the outer depth D_o , outer width B_o , thickness t_o and internal and external corner

Table 1
Measured geometric dimensions for CFDST beam specimens.

Specimen ID	L	B_o	D_o	t_o	$r_{o,ext}$	$r_{o,int}$	D_o/t_o	D_i	t_i	D_i/t_i	$M_{u,test}$	EI_{ini}	Confinement factor	Full model	Moment span model
	(mm)	(mm)	(mm)	(mm)	(mm)	(mm)		(mm)	(mm)		(kNm)	(kNm ²)	ξ_c	$M_{u,FE}/M_{u,test}$	$M_{u,FE}/M_{u,test}$
B-AS120 \times 6-HC22 \times 4-C40	1100	120.5	120.5	5.88	12.5	6.0	20.5	22.0	4.10	5.4	73.1	1290	1.47	0.91	0.92
B-AS120 \times 6-HC22 \times 4-C80	1100	120.2	120.4	5.93	12.5	6.0	20.3	22.1	4.12	5.4	75.9	1340	0.91	0.90	0.91
B-AS120 \times 6-HC22 \times 4-C120	1100	120.2	120.4	5.88	12.5	6.0	20.5	22.2	4.06	5.5	76.3	1260	0.69	0.93	0.95
B-AS120 \times 6-HC32 \times 6-C40	1100	120.2	120.4	5.89	12.5	6.0	20.4	31.9	5.50	5.8	76.3	1230	1.47	0.89	0.91
B-AS120 \times 6-HC32 \times 6-C80	1100	120.2	120.4	5.92	12.5	6.0	20.3	32.0	5.59	5.7	76.0	1380	0.91	0.89	0.92
B-AS120 \times 6-HC32 \times 6-C80R	1100	120.2	120.4	5.93	12.5	6.0	20.3	32.0	5.60	5.7	77.0	1380	0.91	0.89	0.92
B-AS120 \times 6-HC32 \times 6-C120	1100	120.1	120.4	5.89	12.5	6.0	20.5	31.9	5.38	5.9	75.0	1440	0.69	0.93	0.97
B-AS150 \times 3-HC22 \times 4-C40	1100	150.1	150.7	2.79	8.0	5.8	54.0	22.0	4.06	5.4	50.0	1690	0.49	0.97	0.98
B-AS150 \times 3-HC22 \times 4-C40R	1100	150.0	150.6	2.77	8.0	5.8	54.3	22.1	4.06	5.4	50.0	1680	0.48	0.97	0.98
B-AS150 \times 3-HC22 \times 4-C80	1100	150.1	150.6	2.78	8.0	5.8	54.1	22.1	4.06	5.4	55.0	2010	0.30	1.00	1.04
B-AS150 \times 3-HC22 \times 4-C120	1100	150.1	150.7	2.76	8.0	5.8	54.5	22.0	4.01	5.5	57.0	2310	0.23	1.10	1.12
B-AS150 \times 3-HC32 \times 6-C40	1100	150.1	150.7	2.78	8.0	5.8	54.2	31.9	5.42	5.9	52.2	1710	0.48	1.01	1.04
B-AS150 \times 3-HC32 \times 6-C80	1100	150.1	150.7	2.78	8.0	5.8	54.2	32.0	5.47	5.9	58.3	1960	0.30	0.99	1.02
B-AS150 \times 3-HC32 \times 6-C120	1100	150.0	150.7	2.77	8.0	5.8	54.4	31.9	5.57	5.7	57.4	2110	0.23	1.11	1.15
B-AS150 \times 3-HC89 \times 4-C40	1300	150.1	150.5	2.77	8.0	5.8	54.3	88.9	3.91	22.7	78.6	1810	0.48	0.91	0.94
B-AS150 \times 3-HC89 \times 4-C80	1300	150.2	150.7	2.74	8.0	5.8	55.0	88.9	3.92	22.7	79.9	2100	0.29	0.94	0.97
B-AS150 \times 3-HC89 \times 4-C120	1300	150.3	150.8	2.68	8.0	5.8	56.2	89.0	3.91	22.8	83.3	2200	0.22	0.95	0.99
Mean														0.96	0.98
COV														0.071	0.072

radii r_{int} and r_{ext} of the SHS outer tubes, as well as the outer diameter D_i and thickness t_i of the CHS inner tubes, as shown in Table 1.

2.2. Material testing and results

The mechanical properties and full stress–strain response of the adopted steel tubes were obtained by conducting longitudinal tensile tests on coupons extracted from representative regions within the steel cross-sections. The material test setup, procedures and results have been fully described by the authors in Ref. [18], and the results are summarised herein. The acquired full stress–strain curves for the coupons from the inner and outer tubes are shown in Fig. 2, where the suffixes of the cross-section identifiers, ‘F’ and ‘C’, indicate that the coupons were extracted from the flat and corner region of the SHS outer tubes, respectively. The key obtained material properties are reported in Table 2, including the Young's modulus E , the static 0.2% proof and ultimate stresses $\sigma_{0.2}$ and σ_u , the elongation at fracture ϵ_f and the Ramberg-Osgood (R-O) parameters n and m [42,43].

Concrete cylinder tests were performed to obtain the material properties of the concrete infill used in the CFDST beam specimens. Cylinders were cast using the same mix as the corresponding beam specimens and air-cured alongside the specimens under the same environmental conditions. The concrete mixture ingredients and their proportions are presented in Table 4. Concrete cylinder tests were carried out at 28 days after casting and on the days of the respective CFDST beam tests, in accordance with the testing procedures set out in ACI 318 [44]. Table 4 summarises the number of cylinder tests, the mean measured strengths and the corresponding coefficient of variation (COV) values for the three concrete grades.

2.3. Four-point bending tests

Four-point bending tests were conducted to determine the flexural behaviour and capacity of the CFDST cross-sections. A photograph and a schematic diagram of the test rig are depicted in Figs. 3(a) and 3(b), respectively. Two equal vertical loads were applied to the beam specimens by using a spreader beam in a 1000 kN servo-controlled hydraulic testing machine. The beam specimens had a total length of either 1100 or 1300 mm (see Table 3), and were simply supported between two roller supports, which were placed 55 mm inward from each end of the specimen. Magnetic strips were used to fix the roller supports in the prescribed locations during the test preparation and removed before testing. Vertical loads were applied through a half-round and a roller at a

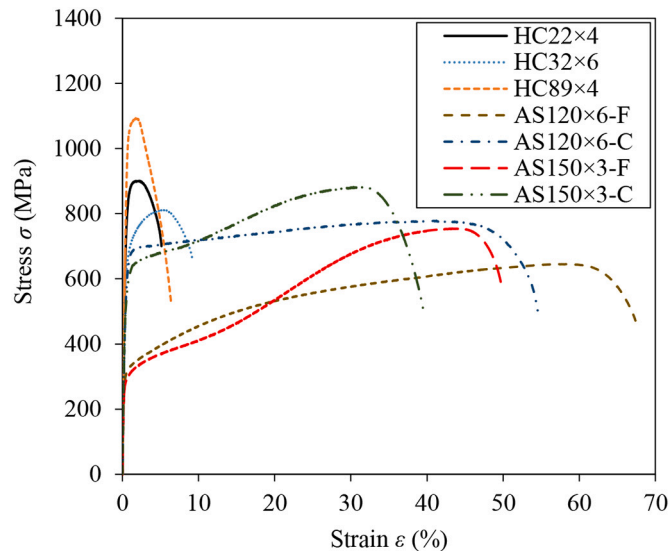


Fig. 2. Stress–strain curves measured from tensile coupon tests [18].

Table 2

Measured material properties obtained from tensile coupon tests [18].

Section	$\sigma_{0.2}$ (MPa)	σ_u (MPa)	E (GPa)	ϵ_f (%)	n	m	$\sigma_u/\sigma_{0.2}$
AS120 × 3-F	287	645	205	67	4	3	2.2
AS120 × 6-C	565	779	187	55	3	4	1.4
AS150 × 3-F	273	754	204	50	4	2	2.8
AS150 × 3-C	518	882	193	40	4	3	1.7
HC22 × 4	794	901	197	5	6	4	1.1
HC32 × 6	619	811	208	9	5	4	1.3
HC89 × 4	1029	1093	209	6	6	4	1.1

distance of 200 mm from the mid-span, thereby attaining a central length of constant moment L_M of 400 mm, as shown in Fig. 3(b). The CFDST beam specimens were locally strengthened at the two loading points by using stiffening plates to mitigate against premature local bearing failure from the concentrated forces. The vertical deflections of the beam specimens at mid-span and the two loading points (denoted as D_M and D_L , respectively) were measured by three 100 mm-stroke Linear Variable Displacement Transducers (LVDTs). The displacement measurements were used to obtain the curvature κ in the constant moment region using Eq. (1) [45].

$$\kappa = \frac{8(D_M - D_L)}{4(D_M - D_L)^2 + L_M^2} \quad (1)$$

All the tests were displacement-controlled with a loading rate equal to 0.2 mm/min until failure. The load, machine displacement and LVDT readings were recorded at 1 s intervals.

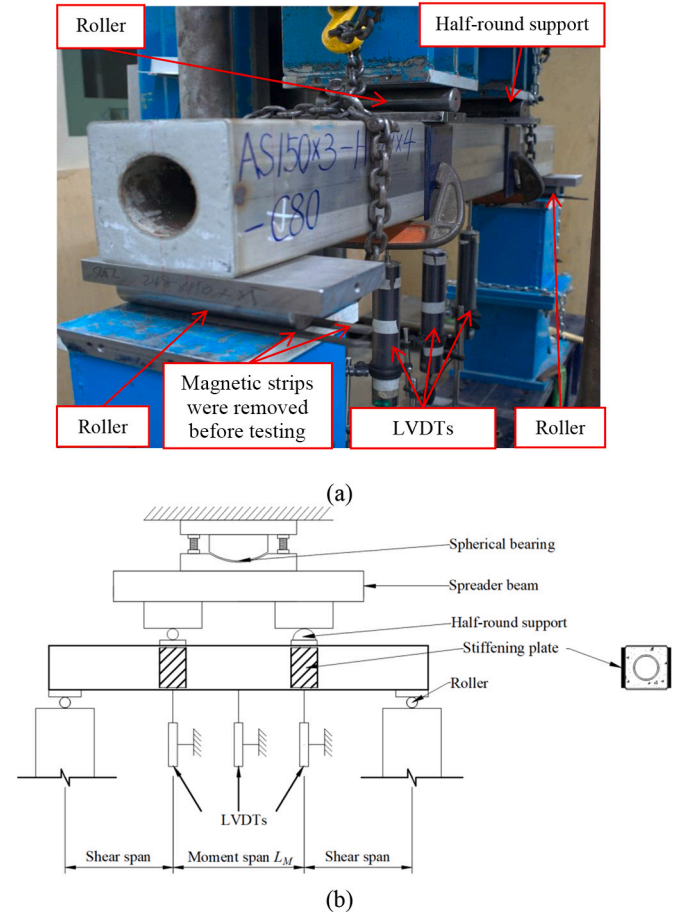


Fig. 3. Experimental setup for CFDST beam specimens: (a) Photograph (AS150 × 3-HS89 × 4-C80); (b) Schematic diagram

Table 3
Concrete mix design.

Concrete grade	Mix proportions (relative to the weight of cement)					
	Cement	Water	Fine aggregate	10 mm aggregate	CSF ^a	SP ^b
C40	1.0	0.56	1.67	2.50	0.000	0.002
C80	1.0	0.32	1.25	1.88	0.000	0.015
C120	1.0	0.21	1.02	1.53	0.087	0.051

Note: ^aCSF = Condensed silica fume; ^bSP = Super plasticizer.

2.4. Test observations

Failure of all the tested CFDST beams featured outward local buckling of the stainless steel SHS outer tube, cracking and crushing of the concrete infill and some ovalisation and inward local buckling of the high strength steel CHS inner tube within the constant moment region, as shown in Fig. 4 for a typical tested specimen B-AS150 × 3-HC89 × 4-C120. The derived moment–curvature characteristics of all the specimens are depicted in Fig. 5, grouped by CFDST cross-section to enable direct comparisons among specimens with varying concrete grades. All the curves displayed rounded and ductile behaviour, reflecting, in part, the nonlinear and ductile stress-strain response and pronounced strain hardening of the stainless steel outer tubes [14]. It is also evident that, for the same CFDST cross-section, an increase in the concrete strength resulted in rather limited enhancements in moment capacity; this observation mirrors the findings for CFST beams reported in [35,46]. The key test results are summarised in Table 1 for each CFDST beam, including the experimental failure moment $M_{u, test}$ and the initial flexural stiffness EI_{ini} . Note that the peak values of the moment were not attained for specimens with CFDST cross-sections AS120 × 3-HC22 × 4 and AS120 × 3-HC32 × 6, since the moment–curvature curves were still rising despite large curvatures. For these specimens, the failure moment was defined as the bending moment at which the tangent stiffness of the moment–curvature curve at increment i , EL_i , dropped to 1% of the initial stiffness, EL_{ini} , — i.e. failure was taken at the point where $EL_i/EL_{ini} = 0.01$, an example of which is presented in Fig. 6. Details of this approach were described by the authors in [39] for application to CFDST cross-sections with CHS stainless outer tubes, and the basis was explained in [47]. It is worth noting that, for the specimens that did reach their peak moment, the difference between the measured peak moment and the moment at which $EL_i/EL_{ini} = 0.01$ was found to be minimal (<3%). Hence, for consistency, the 1% tangent stiffness definition of the failure moment has been applied to all the test and FE specimens herein.

3. Numerical modelling

3.1. Development of FE model

A comprehensive numerical modelling programme was performed employing the general-purpose finite element (FE) analysis package ABAQUS [48]. A validation study was first conducted, where FE models were developed based on the measured geometric dimensions of the test specimens reported in Table 2. Computational efficiency was sought by exploiting symmetry about the mid-span plane of the beams and the

Table 4
Measured concrete cylinder strengths.

Concrete grade	Cylinder tests at 28 days			Cylinder tests at days of CFDST beam tests		
	No. of tests	Mean (MPa)	COV	No. of tests	Mean (MPa)	COV
C40	5	36.6	0.058	7	43.1	0.017
C80	6	76.3	0.022	5	84.7	0.017
C120	5	111.2	0.043	6	114.1	0.033

Table 5

Cross-section dimensions and material properties of CFDST beams chosen for parametric study.

$B_o \times D_o \times t_o$	$\sigma_{0.2,o}$	$D_i \times t_i$	$\sigma_{0.2,i}$	f_c
(mm × mm × mm)	(MPa)	(mm × mm)	(MPa)	(MPa)
600 × 600 × 60, 600 × 600 × 40,	287	300 × 15, 300 × 10,	619	40,
600 × 600 × 30, 600 × 600 × 24,				
600 × 600 × 20, 600 × 600 × 15,				
600 × 600 × 12, 600 × 600 × 10,				
600 × 600 × 9, 600 × 600 × 8, 600 × 600 × 7, 600 × 600 × 6				
		3, 300 × 2	1029	120

plane perpendicular to the axis of bending—hence, only one quarter of the beam specimens were modelled with suitable boundary conditions assigned to the planes of symmetry, as shown in Fig. 7 (a). C3D8R solid elements were used for the concrete infill and S4R shell elements were adopted for the metal tubes, in line with previous numerical simulations of concrete-filled tubular members [17,20,48–51]. In the one-quarter models, the elements of the stiffened region at the loading point were coupled to a reference point (denoted R_L), and the elements at the roller support region were coupled to another reference point (denoted R_S). The four-point bending configuration employed in the tests was thus achieved by applying suitable boundary conditions to the reference points, as detailed in Fig. 7(a). The displacement-controlled testing procedure was simulated by imposing vertical displacements at R_L . A prior mesh sensitivity study was undertaken to decide upon suitable mesh densities for each constituent component of the models, in order to produce accurate yet computationally efficient results. For the SHS outer tubes, the corner regions were uniformly discretised into at least four elements to allow the curved corner geometry to be captured, while the flat regions were modelled with an element size equal to the respective thickness of the SHS tube. A uniform mesh seed size of $\pi D_i/40$ was chosen for the CHS inner tubes. For the sandwiched concrete, the element sizes were selected to be generally consistent with those of the adjacent tubes to facilitate numerical convergence. As for the mesh density in the longitudinal direction, a finer mesh was applied within the moment span where failure was expected, while a coarser mesh was adopted for the remainder of the FE model. For modelling convenience, FE beam models under pure bending moment (denoted as moment span models) were also developed and compared with the results from the tests and full models. The moment span model was developed using the same mesh settings as those adopted in the full model, but with a length equal to the constant moment span L_M . The two end sections were coupled to two reference points, which were allowed to rotate in the direction of bending, as shown in Fig. 7(b).

For the constitutive modelling of the examined CFDST beams, the approach employed by the authors in previous numerical investigations into the compressive behaviour of equivalent CFDST cross-sections was generally followed [18]. A detailed description of these constitutive models is provided in [18], and only the key aspects are reported herein. For the outer and inner steel tubes, the true stress–logarithmic plastic strain curves derived from measured engineering stress–strain curves were adopted, as required in ABAQUS. For the concrete infill, both the compressive and tensile properties were defined within a concrete damage plasticity (CDP) model [48]. A confined concrete stress–strain curve was adopted to take due account of the confinement afforded to the concrete, which was derived by calibration against test data on carbon steel CFST stub columns in Tao et al. [52]. Modifications were made by the authors [17,18] for application to CFDST cross-sections with stainless steel outer tubes. The modifications were concerned primarily with the confinement factor (ξ_c) [1,45], defined in Eq. (2),

$$\xi_c = \frac{A_o \sigma_{0.2,o}}{A_{ce} f_c} \quad (2)$$

Table 6
Limitations on material strengths in design codes.

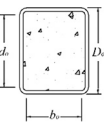
Concrete-filled steel tubular cross-section	Design codes	Cross-sectional slenderness	Limitation	$\sigma_{0.2}$ (MPa)	f_c (MPa)
	EN 1994-1-1	D_o/t_o	$D_o/t_o \leq 52 \sqrt{\frac{235}{\sigma_{0.2,o}} \frac{E_o}{210000}}$	235–460	20–50
	AISC 360	b_o/t_o	Compact		
		d_o/t_o	Noncompact		
			Maximum		
			λ_p	≤ 525	21–70
			λ_r		
			$2.26(E_o/\sigma_{0.2,o})^{0.5}$		
			$3.00(E_o/\sigma_{0.2,o})^{0.5}$		
			$3.00(E_o/\sigma_{0.2,o})^{0.5}$		
			$5.70(E_o/\sigma_{0.2,o})^{0.5}$		
			$5.70(E_o/\sigma_{0.2,o})^{0.5}$		

Table 7
Comparisons of test and FE ultimate moments with predicted moment resistances from EC4 and AISC 360–16.

Design codes	Section type	No. of results		M_u/M_{code}	
		Test	FE	Mean	COV
EC4	Falling within the EC4 limit	7	80	1.86	0.158
	Falling outside the EC4 limit	10	109	1.35	0.126
	Total	17	189	1.57	0.218
EC4*	Falling within the EC4 limit	7	80	1.86	0.158
	Falling outside the EC4 limit	10	109	1.56	0.084
	Total	17	189	1.69	0.160
AISC 360	Compact	17	100	1.77	0.185
	Noncompact	0	50	1.49	0.085
	Slender	0	39	1.89	0.054
	Total	17	189	1.72	0.171

Table 8
Comparison of test and FE strengths with design predictions based on plastic moment resistances for specimens falling within their respective codified slenderness limits.

f_c (MPa)		Ratio of test-to-predicted strengths			
		M_u/M_{EC4}	M_u/M_{EC4*}	M_u/M_{AISC}	M_u/M_{AISC*}
40	Mean	1.97	1.97	1.81	1.81
	COV	0.139	0.139	0.185	0.185
80	Mean	1.90	1.93	1.77	1.80
	COV	0.135	0.132	0.189	0.182
120	Mean	1.87	1.91	1.75	1.79
	COV	0.130	0.126	0.177	0.171
Sum	Mean	1.91	1.94	1.78	1.80
	COV	0.134	0.131	0.182	0.177

where A_{ce} is an equivalent cross-sectional area of concrete, defined as the full area enclosed by the outer tube, as given by Eq. (3).

$$A_{ce} = (D_o - 2t_o)^2 - (4 - \pi)r_{int}^2 \quad (3)$$

The confinement factor for each beam specimen is presented in Table 1. The tensile properties of the concrete were characterised by a linear response up to the ultimate tensile strength, taken as $0.1f_c$, and a descending branch defined by the fracture energy G_F [52].

The interfaces between the metal tubes and sandwiched concrete were modelled by means of surface-to-surface contact in ABAQUS [48]. “Hard contact” was employed in the normal direction, while a Coulomb friction model with a friction coefficient of 0.6 was adopted in the tangential direction [17,53]. Residual stresses and initial local geometric imperfections have negligible influence on the ultimate response of CFDST beams, owing principally to the fact that the support afforded to the tubes from the concrete infill lessens the sensitivity of the tubes to local stabilities. Therefore, the inclusion of the local imperfections and residual stresses was deemed to be unnecessary; the suitability of this treatment is confirmed by the successful validation of the FE model against the test results in the next subsection.

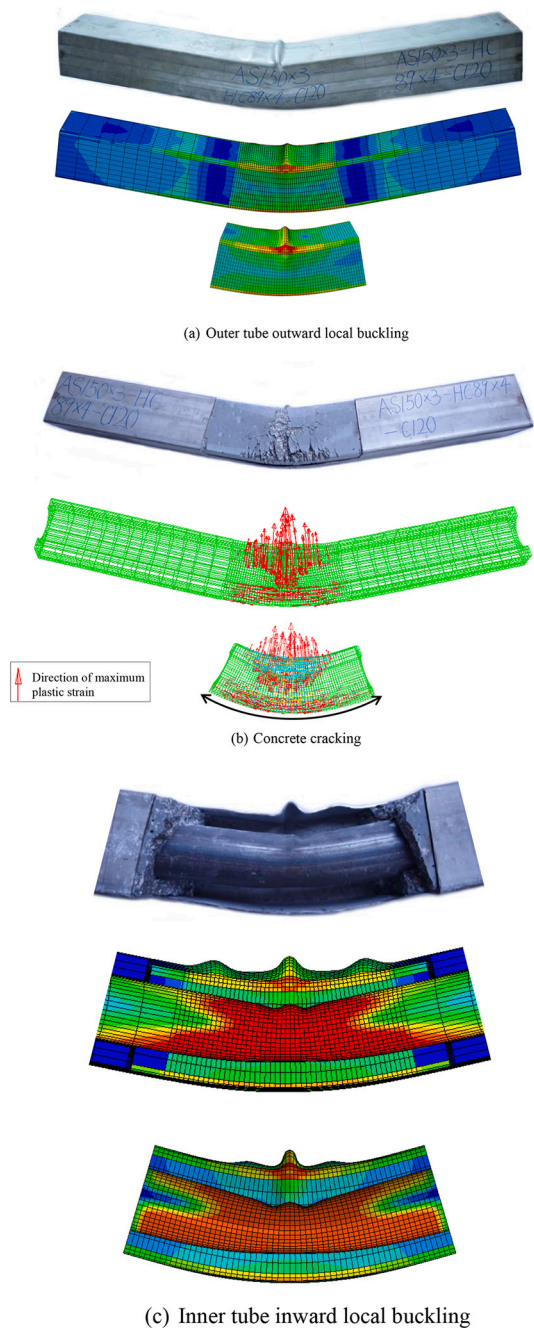


Fig. 4. Experimental and numerical failure modes of CFDST beam specimen B-AS150 × 3-HC89 × 4-C120.

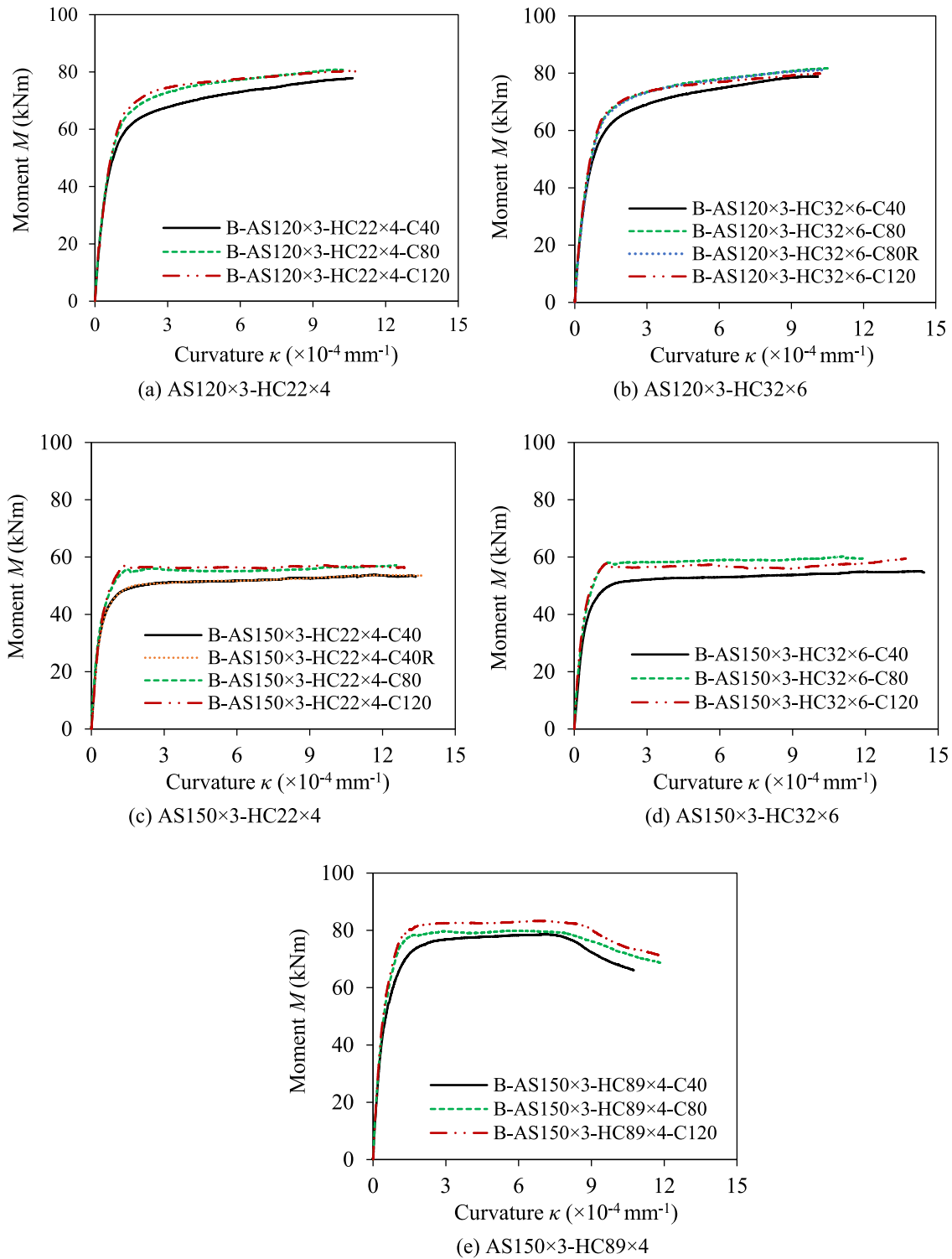


Fig. 5. Moment–curvature curves of the test CFDST beam specimens.

3.2. Validation of FE model

The accuracy of the developed full model and moment span model was affirmed by comparing the numerically acquired moment-curvature curves, failure modes and failure moments against the test observations presented in Section 2. Good agreement was achieved between the moment–curvature curves obtained from the tests, the full FE model and the moment span FE model, as shown for a typical CFDST beam specimen B-AS150 × 3-HC89 × 4-C40 in Fig. 8. It can be observed that the

initial stiffness, failure moment and the rounded and ductile load-deformation history are fully captured by the FE simulations from both FE models. The experimental failure modes for the metal tubes and concrete infill are also successfully reproduced by their FE counterparts, as shown in Fig. 4. The numerical to experimental failure moment ratios $M_{u,FE}/M_{u,test}$ are reported in Table 1 for both the full FE model and moment span FE model, showing mean values of $M_{u,FE}/M_{u,test}$ equal to 0.96 and 0.98 and corresponding COV values of 0.071 and 0.072, respectively. This reveals that the developed full FE model and moment

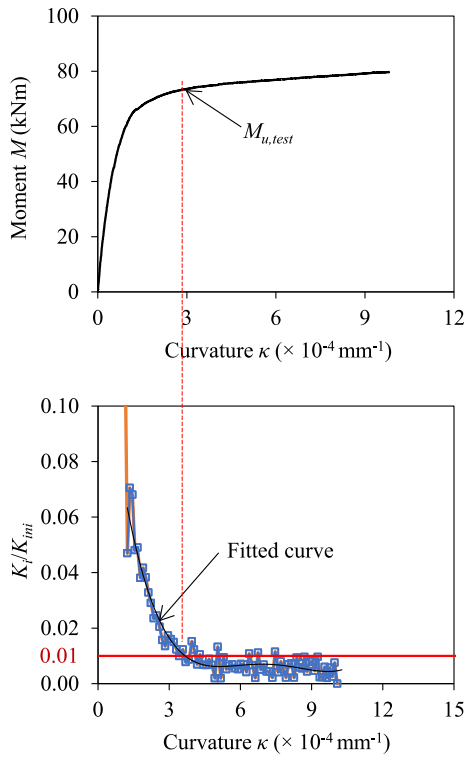


Fig. 6. Definition of experimental failure moment $M_{u,test}$ at $K_t/K_{int} = 0.01$.

span FE model yield a high degree of accuracy and consistency in predicting the experimental failure moments. Overall, results from both the full span FE model and the moment span FE model were found to match well with the corresponding test observations. The moment span model was chosen in the following parametric study considering its simplicity in modelling and the ease in obtaining the moment contribution from each component, as illustrated by some typical examples in Fig. 9.

3.3. Parametric study

Having validated the moment span FE model against the test data, a parametric study was conducted to expand the test dataset over a broader range of cross-section dimensions and material strengths. Table 5 summarises the key parameters of the CFDST beam FE model, where it is shown that 12 different SHS were employed for the outer tube and 5 different CHS tube were employed for the inner tube. The outer tube was assigned the material properties of the tested stainless steel AS120 × 6, while three different high strength steel materials, with yield strengths varying from 619 to 1029 MPa were employed for the inner tube. The cylinder compressive strength of the sandwiched concrete was varied from 40 to 120 MPa. The moment spans of all the modelled CFDST beams were set equal to 1500 mm. Note that the cross-sectional slenderness of the modelled CFDST beams was determined by the local slenderness of the outer tube, in line with the definition for CFST members in the European Code EN 1994-1-1 [40] and American Specification AISC 360-16 [41], as shown in Table 6. The modelled CFDST beam specimens were chosen to extend beyond the current maximum slenderness limit of EN 1994-1-1 [40] and covered compact, non-compact and slender sections according to the classification limits for composite sections prescribed in AISC 360-16 [41]. Overall, a total of 189 numerical parametric results on CFDST beams were produced. Combined with the test results reported in Section 2, the full data set generated in this study is employed to evaluate the applicability of existing design rules to the examined CFDST cross-sections in Section 4.

4. Discussion of current design methods

4.1. General

CFDST members fall into the general category of concrete-filled tubular structures, which are designed in accordance with the provisions set out in EN 1994-1-1 (EC4) [40] and AISC 360-16 [41]. In this study, the relevant design provisions of EN 1994-1-1 and AISC 360-16 are first described in Section 4.2 and 4.3, respectively; the applicability of these provisions to the studied CFDST beams is appraised in Sections 4.4, and modifications to the existing design rules are proposed and evaluated in Section 4.5.

Note that, in the comparisons presented, the measured/modelled material properties and geometric dimensions of the test/FE specimens have been employed, and all partial safety factors have been taken equal to unity. Limitations on material strengths stipulated in the examined design codes are provided in Table 6, which are exceeded for some of the tested and modelled specimens; comparisons and evaluations are still presented to explore possible extension of the codes beyond their current range of applicability.

4.2. EN 1994-1-1 (EC4)

The moment resistance of square concrete-filled steel tubular cross-sections in EN 1994-1-1 [40] is calculated assuming a fully plastic stress distribution over the entire cross-section [40]. The analogous stress distribution for the studied CFDST cross-sections is illustrated in Fig. 10(a), where the yield stresses $\sigma_{0.2,o}$ and $\sigma_{0.2,i}$ are allowed to develop across the full stainless steel outer tube and high strength steel inner tube in both compression and tension; the tensile strength of the concrete is neglected as a result of concrete cracking prior to the attainment of the failure moment, while the compressive stresses in the concrete infill are taken as the compressive concrete cylinder strength f_c to take due account of the confinement afforded by the outer tube. The position of the neutral axis is determined using a fibre analysis approach, which has been previously adopted by the authors in the study of circular CFDST members in flexure [39] and a brief summary is described herein. The cross-section is first discretised evenly into a total of 1000 horizontal fibres, as shown in Fig. 11, with the position of the neutral axis (y) assumed at an initial location at fibre i . The overall axial force F is thus obtained by summing the axial forces in the outer and inner tubes and the concrete infill, denoted as F_o , F_i and F_c , which can be determined by integrating the corresponding stress distributions over the respective areas with reference to the assumed neutral axis location y . The location of the neutral axis is changed incrementally to fibre $i + 1$ until F reaches zero, indicating that axial force equilibrium has been achieved and hence the neutral axis position has been identified. Upon determination of the position of the neutral axis, the bending moment resistance M_{EC4} can be subsequently obtained.

A maximum cross-section slenderness limit of $D_o/t_o \leq 52(235/f_y)$ is prescribed in EC4 for square/rectangular concrete-filled composite members. A slightly modified version of this slenderness limit is proposed for application to stainless steel to reflect the difference in Young's modulus relative to carbon steel, as given by $D_o/t_o \leq 52\sqrt{(235/\sigma_{0.2,o})(E_o/210000)}$. Possible relaxation of this slenderness limit is assessed in Section 4.4.

4.3. American specification AISC 360-16

AISC 360-16 [41] adopts the cross-section classification concept and defines corresponding stress distributions for calculating the bending moment resistance of CFST cross-sections. Three classes of CFST cross-section are defined in AISC 360-16 [41], namely compact, non-compact and slender sections. Classification of a square CFST cross-section is made according to the class of the most slender constituent

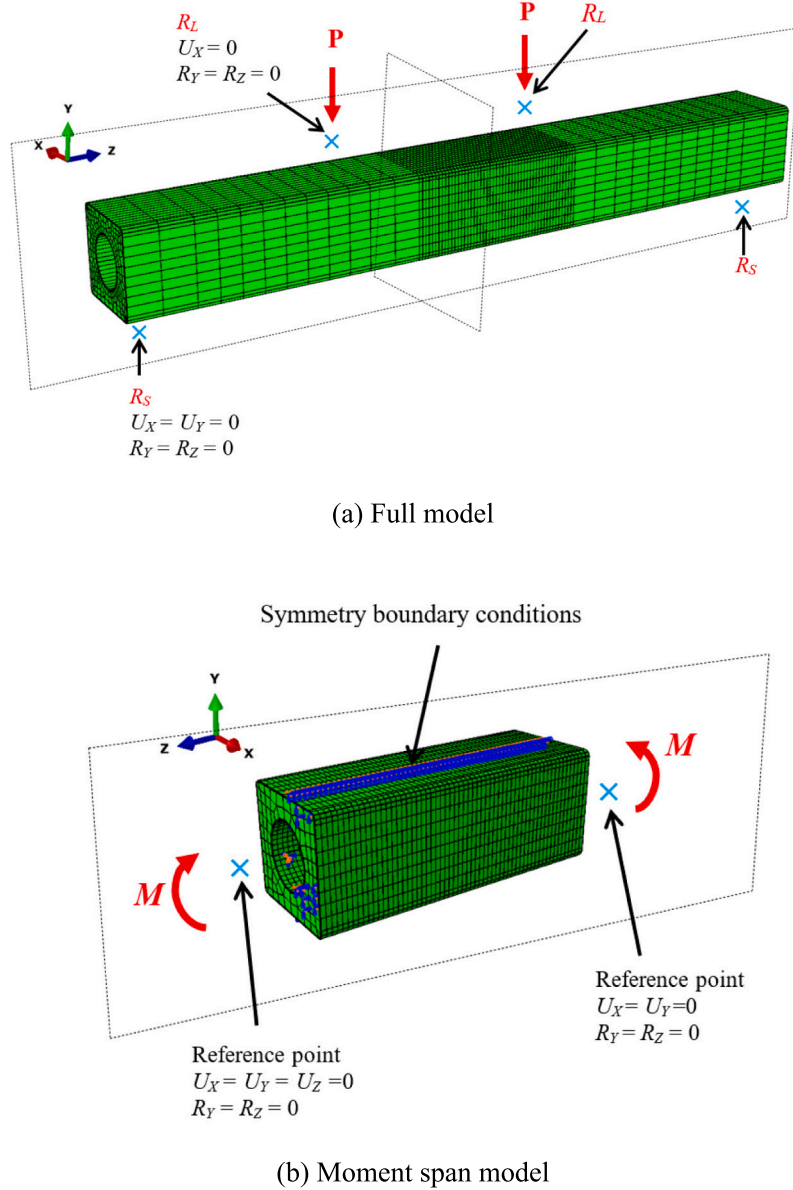


Fig. 7. CFDST beam FE models in ABAQUS.

plate element of the SHS tube, while each constituent plate element is classified by comparing its local slenderness λ , defined as b_o/t_o for the flange and d_o/t_o for the web against the prescribed slenderness limits (i. e. the compact/noncompact limit λ_p and the noncompact/slender limit λ_r), where b_o and d_o are taken as the flat widths of the elements excluding the corner radii for the flange and web of SHS outer tube, respectively, as shown in Table 6.

The AISC 360–16 [41] bending moment resistances M_{AISC} for the studied CFDST cross-sections were determined with reference to the above slenderness limits (modified for application to stainless steel), and are listed in Table 6. Compact sections are capable of attaining their full plastic moment capacity M_p ; AISC 360–16 [41] adopts a similar plastic stress distribution to that defined in EC4 [40], but with a slightly lower confinement coefficient of 0.95 for the compressive stress f_c , as shown in Fig. 10(a). As for noncompact sections, the full plastic moment capacity cannot be achieved as a result of local buckling in the outer tube; instead, the moment resistance of a noncompact cross-section is calculated based on a partial plastic stress distribution, with the degree of spread of plasticity dependent on the cross-section slenderness λ .

Specifically, the moment resistance is determined by linear interpolation between the plastic moment capacity M_p and the yield moment capacity M_y with respect to the cross-section slenderness λ , bound by the compact and noncompact slenderness limits of $2.66(E_o/\sigma_{0.2,o})^{0.5}$ and $3.00(E_o/\sigma_{0.2,o})^{0.5}$ respectively, as given by Eq. (4),

$$M_{AISC} = \begin{cases} M_p & \text{for compact sections} \\ M_p - \frac{M_p - M_y}{(\lambda_r - \lambda_p)} (\lambda - \lambda_p) & \text{for noncompact sections} \\ M_{cr} & \text{for slender sections} \end{cases} \quad (4)$$

where M_y is the first yield moment, assuming a linear elastic stress distribution with the maximum compressive stress limited to the yield stress $\sigma_{0.2,o}$ at the extreme fibre of the outer tube and to $0.7f_c$ within the concrete. The stress distribution in the inner tube is derived on the basis of strain compatibility, controlled by the compressive fibre of the outer tube being at the yield strain $\epsilon_y = \sigma_{0.2,o}/E_o$, as shown in Fig. 10(b). For slender sections, the moment resistance (M_{cr}) is determined using a similar stress distribution as that for noncompact sections, but the outer

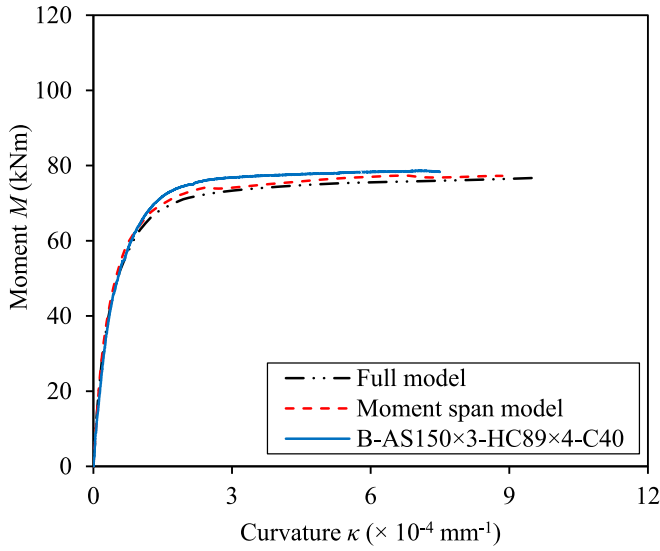


Fig. 8. Comparisons of moment-curvature curves from test and FE models.

tube is limited to linear elastic behaviour in both tension and compression, with the respective maximum stress at the extreme fibre equal to the yield stress $\sigma_{0.2,o}$ and the elastic critical local buckling stress f_{cr} , given by $9E_o/(b_o/t_o)^2$, as shown in Fig. 10(c). These limitations are set to reflect the fact that the flange of the outer tube in a slender cross-section is prone to local buckling prior to reaching the material yield stress, thereby restricting the spread of plasticity in the outer tube. Fig. 10 depicts an overview of the state of plasticity in the outer tube of cross-sections of different classes. Fig. 12 illustrates the variation in bending moment resistance from AISC 360–16 (M_{AISC}) with local slenderness λ for compact, noncompact and slender CFDST beams.

4.4. Assessment of current design methods

The accuracy of the bending moment resistance predictions from EC4 (M_{EC4}) and AISC 360–16 (M_{AISC}) is evaluated by making comparisons against the test/FE failure moment capacities M_u . Numerical comparisons are provided in Table 7, while graphical comparisons are shown in Figs. 13 and 14, where the ratios of M_u/M_{code} are plotted against the corresponding normalised cross-section slenderness, i.e. $\lambda_{EC} = D_o/t_o \epsilon$, in which $\epsilon = \sqrt{(235/\sigma_{0.2,o})(E_o/210000)}$, and $\lambda_{AISC} = b_o/t_o(\sigma_{0.2,o}/E_o)^{0.5}$. Significant conservatism and scatter were found for CFDST cross-sections falling within the modified EC4 slenderness limits and for compact sections defined by AISC 360, where a general trend of increasing conservatism with decreasing λ values was observed. The underestimated bending resistances in the lower slenderness domain are attributed to the lack of account taken for strain hardening in the metal tubes, particularly the stainless steel outer tubes [54–56], as well as the higher degree of confinement afforded by the stockier outer tubes to the concrete infill. The underestimation was more obvious for AISC 360–16 [41] in comparison with EN 1994-1-1 [40], due mainly to the lower concrete confinement coefficient used for the concrete in compression. For the CFDST cross-sections that lie beyond $\lambda_{EC} = 52$, the resistance predictions from EC4 become less conservative and more scattered, with some results on the unsafe side, indicating that these CFDST cross-sections are unable to achieve their full plastic moment capacities. This may be attributed to the occurrence of local buckling of the outer tubes prior to the development of full plasticity and the consequential reduced confinement afforded to the concrete infill. Conversely, the conservatism of the AISC 360–16 design predictions increases with increasing slenderness for the noncompact and slender sections, indicating that AISC 360–16 may underestimate the spread of plasticity in the metal tubes and the level of confinement afforded to the concrete in these slenderness ranges. Overall, the mean ratios of M_u/M_{code} are equal to 1.57 and 1.72, with COV values equal to 0.218 and 0.171 for EC4 [40]

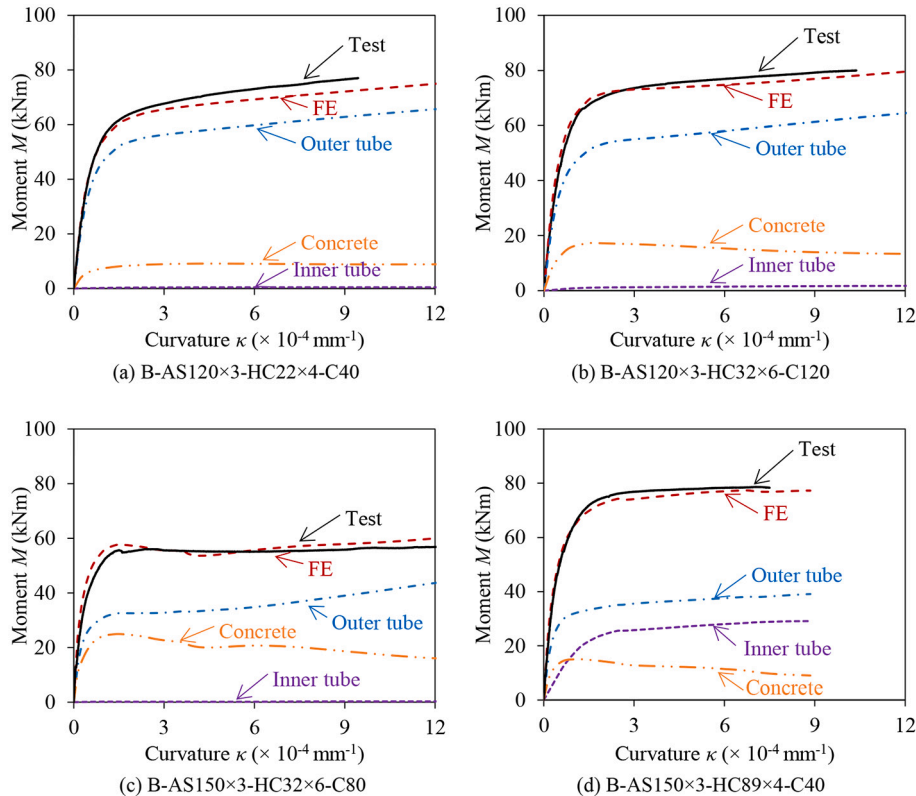
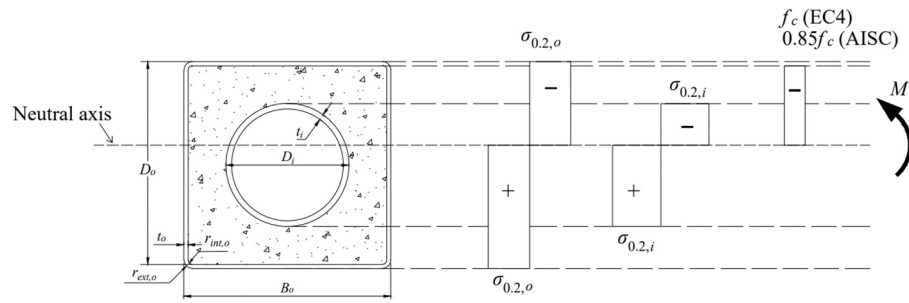
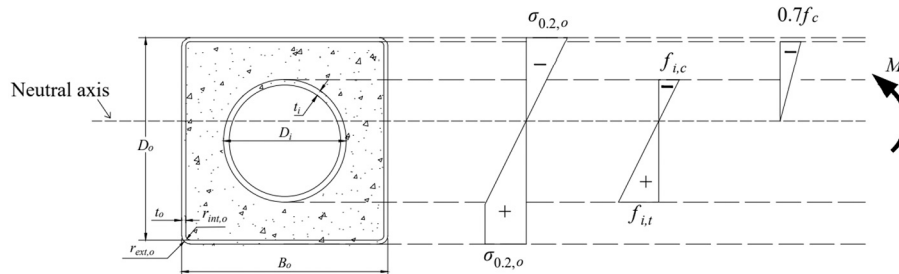
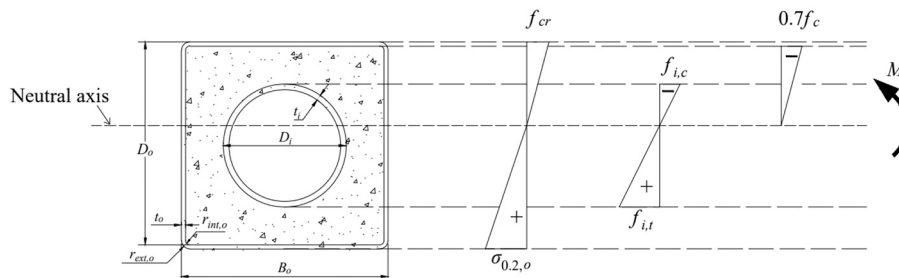
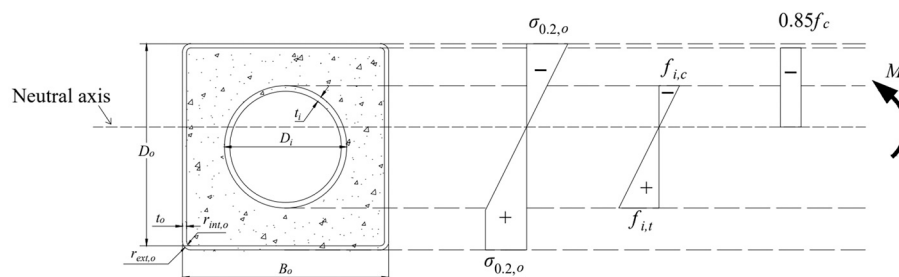


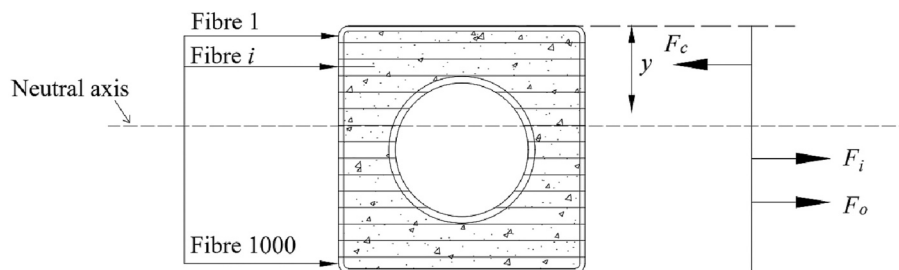
Fig. 9. Comparisons of test and FE moment-curvature curves for typical CFDST beam specimens.



(a) EC4 and compact sections in AISC 360

(b) Determination of M_y in AISC 360(c) Determination of M_{cr} for slender sections in AISC 360

(d) Proposal for sections falling outside the slenderness limit in EC4

Fig. 10. Stress distributions for determining bending moment resistances of CFDST cross-sections.**Fig. 11.** Fibre analysis approach for determining position of neutral axis of CFDST cross-section in bending (when $F_c + F_i + F_o = 0$).

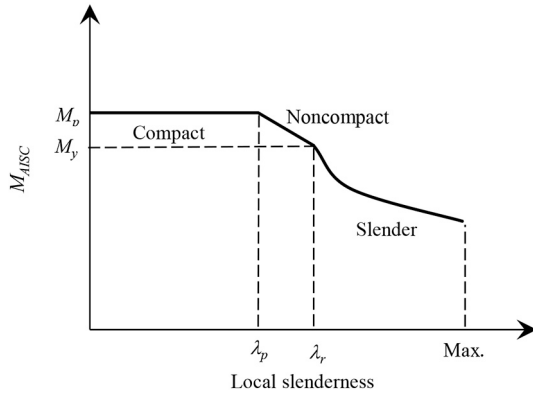


Fig. 12. Moment resistance predicted from AISC 360 (M_{AISC}) versus local slenderness for CFDST beams.

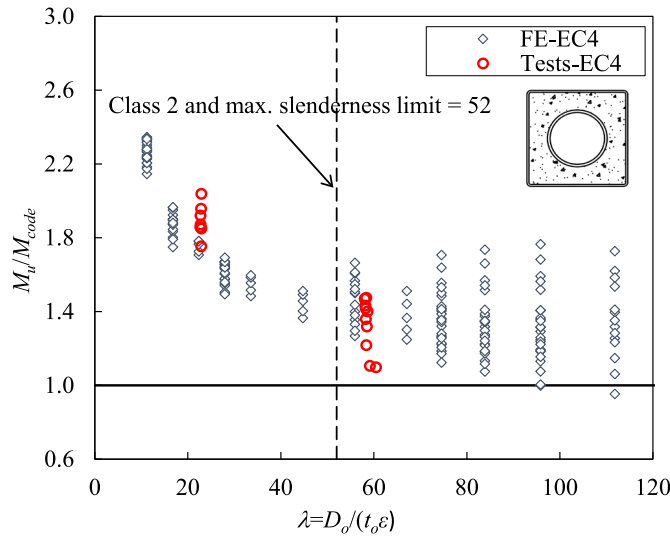


Fig. 13. Comparisons of test and FE results with moment resistance predictions from EC4.

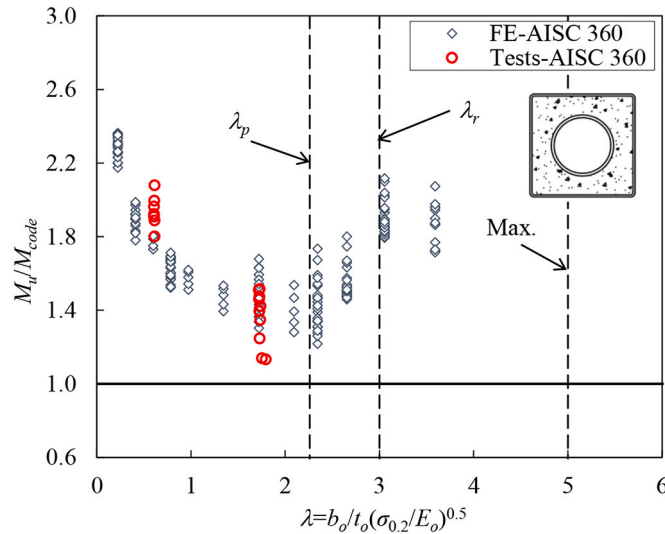


Fig. 14. Comparisons of test and FE results with moment resistance predictions from AISC 360-16.

and AISC 360-16 [41], respectively, as shown in Table 7. The comparisons reveal that the current design rules in EC4 [40] and AISC 360-16 [41] generally yield conservative and scattered moment resistance predictions when applied to CFDST cross-sections with stainless steel outer tubes.

4.5. Modifications to design rules

4.5.1. Modifications for high strength concrete

The bending moment resistance design predictions of the CFDST cross-sections with lower grade concrete were found to be more conservative than their counterparts with higher grade concrete, as shown in Table 8, indicating that the degree of influence of the concrete strength on the moment capacities differs among the concrete grades. This is because the effectiveness of the confinement afforded to high strength concrete is essentially lower than their normal strength counterparts. These observations have been previously made for CFST members [57] and also echo the findings for the equivalent CFDST cross-sections in compression [18]. To reflect the difference in determining the plastic moment capacities of the CFDST cross-sections studied herein, the concrete strengths were multiplied by a reduction factor η , as specified in EN 1990-1-1 [58] and given by Eq. (5), to account for the effective compressive strength of high grade concrete up to 90 MPa, beyond which a constant value of 0.8, as proposed by Liew et al. [57], is employed.

$$\eta = \begin{cases} 1.0 - \frac{f_c - 50}{200} & 50 \text{ MPa} < f_c \leq 90 \text{ MPa} \\ 0.8 & f_c > 90 \text{ MPa} \end{cases} \quad (5)$$

The accuracy of the modified EC4 and AISC 360-16 capacity predictions (denoted as M_{EC4*} and M_{AISC*}) is assessed in the graphical comparisons shown in Fig. 15, revealing that the inclusion of η in the design calculations yield more consistent and less scattered design moment capacity predictions for the examined CFDST beams. The improved consistency is also shown quantitatively by the reduced COV values across the range of concrete grades from C40 to C120 in Table 8.

4.5.2. Modifications to bending resistance calculation

It was found that the current EC4 design approach yielded excessively scattered moment resistance predictions for CFDST cross-sections beyond the maximum slenderness limit of $\lambda_{EC} = 52$, with some predictions on the unsafe side. This is owing to the fact that the full plastic moment capacities could not be consistently attained for $\lambda_{EC} > 52$. To rectify this, a modified stress distribution, considering only the partial spread of plasticity over the whole section, is developed herein, as shown in Fig. 10(d). The stress distribution in the stainless steel outer tube is bilinear in the tension region and linear in the compression region; this results from the failure definition based on first yield in compression, i.e., plastic reserves in the tension region may be exploited until the onset of yielding at the extreme compressive fibre. The stress distribution in the inner tube is determined by strain compatibility with respect to first yield of the outer tube. As for the concrete infill, due account of the reduced effectiveness of the steel tube in confining the concrete due to local buckling for $\lambda_{EC} > 52$ is taken by using a lower confinement coefficient of 0.85.

In order to assess the accuracy of the modified EC4 design approach for the CFDST cross-sections beyond the maximum slenderness limit of $\lambda_{EC} = 52$, the obtained test/FE failure moment capacities M_u are normalised by the modified EC4 failure moment predictions M_{EC4*} , and plotted against the cross-section slenderness λ_{EC} in Fig. 16. The statistical results, in the form of the mean and COV values of M_u/M_{EC4*} , are summarised in Table 7. It can be seen that the modified EC4 design approach provides conservative moment predictions and significantly improves design consistency for CFDST cross-sections falling outside the current EC4 limit. Together with the inclusion of the concrete strength

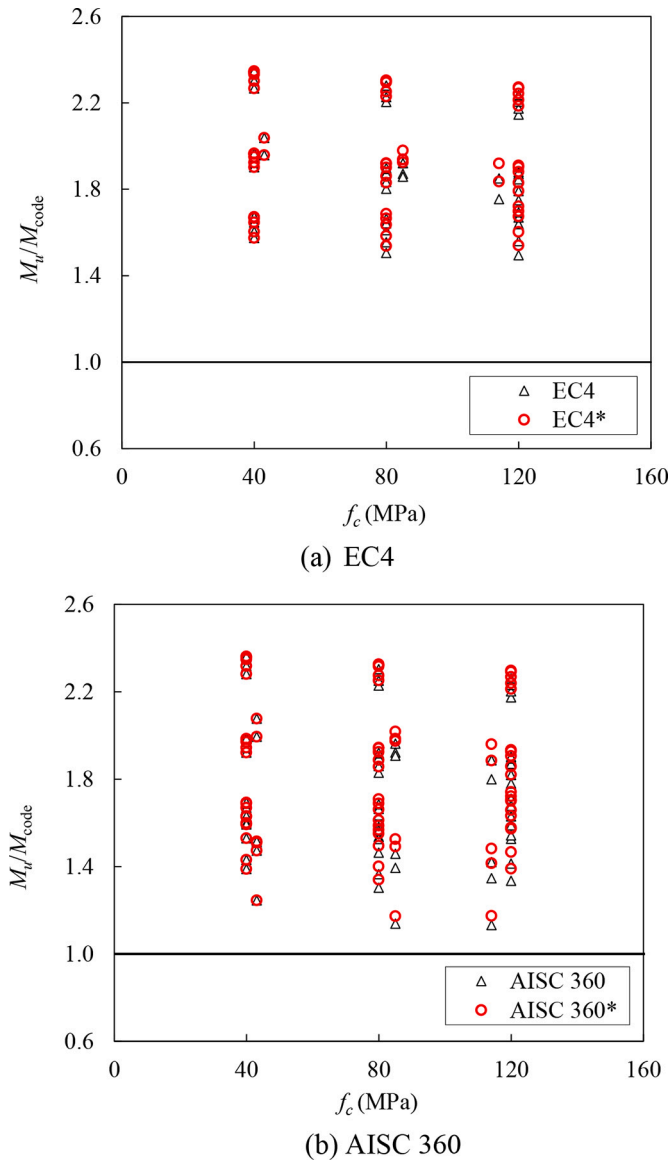


Fig. 15. Comparisons of test and FE results with current and modified moment resistance predictions from design codes.

reduction factor modified for CFDST cross-sections falling within the current EC4 limit, the modified EC4 design proposal can be safely applied to the design of CFDST beams across a wide range of cross-section slenderness values.

5. Conclusions

Laboratory testing and numerical modelling have been conducted to investigate the structural performance of CFDST cross-sections with stainless steel SHS outer tubes and high strength steel CHS inner tubes in bending. A total of 17 four-point bending tests was performed on five CFDST cross-sections with varying concrete grades, and their moment capacities, moment–curvature curves and failure modes are fully described. Finite element models were then developed and validated with reference to the test results. Parametric studies were subsequently carried out, generating a total of 189 additional results over an extended range of material strengths and cross-section slendernesses. The general design provisions for concrete-filled carbon steel members in EN 1994-1-1 [40] and AISC-360-16 [41] were assessed for application to the studied CFDST cross-sections. On the basis of the graphical and quantitative

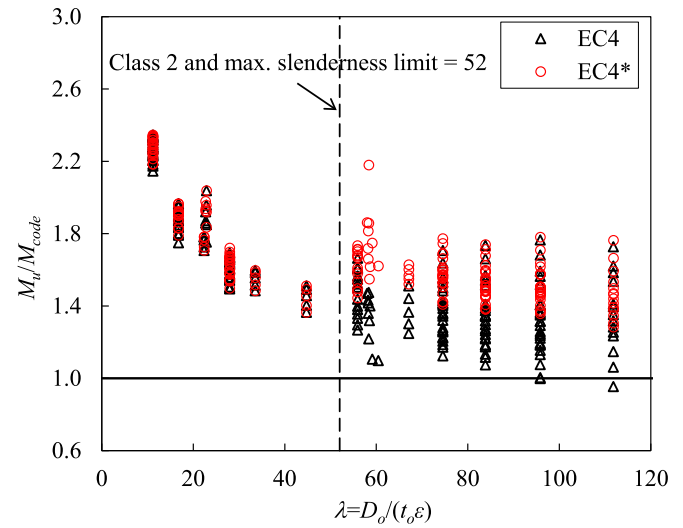


Fig. 16. Comparisons of test and FE results with moment resistance predictions from modified EC4.

assessment results, it is concluded that (i) EN 1994-1-1 [40] offers conservative and scattered moment resistance predictions for cross-sections falling within the maximum cross-section slenderness limits, beyond which the predictions are slightly unconservative and unduly scattered, and (ii) AISC 360-16 [41] generally results in a higher degree of conservatism and scatter than EN 1994-1-1 [40]. Modifications to the current EN 1994-1-1 [40] provisions are proposed—a concrete strength reduction factor η to reflect the reduced relative effectiveness of using higher concrete grades and a modified stress distribution considering the partial spread of plasticity for CFDST cross-sections beyond the current maximum slenderness limit. Comparisons with the test/FE results demonstrated that the modified design rules offer conservative results with improved consistency across a wide range of cross-section slenderness values.

CRedit authorship contribution statement

Fangying Wang: Conceptualization, Methodology, Software, Data curation, Formal analysis, Investigation, Writing – original draft, Visualization. **Ben Young:** Conceptualization, Methodology, Supervision, Writing – review & editing, Funding acquisition, Project administration. **Leroy Gardner:** Conceptualization, Methodology, Supervision, Writing – review & editing.

Declaration of Competing Interest

The authors declare that they have no known competing financial interests or personal relationships that could have appeared to influence the work reported in this paper.

The authors declare the following financial interests/personal relationships which may be considered as potential competing interests:

Co-author (Ben Young) is the Editors-in-Chief of JCSR.

Data availability

Data will be made available on request.

Acknowledgements

The authors would like to acknowledge the contribution of Mr. Cheuk Him Wong and Mr. Chi Hang Tik for their support in the experimental programme. The authors are grateful to Stalatube Oy, Finland for supplying the test specimens.

References

- [1] L.-H. Han, W. Li, R. Bjorhovde, Developments and advanced applications of concrete-filled steel tubular (CFST) structures: members, *J. Constr. Steel Res.* 100 (2014) 211–228.
- [2] M.L. Romero, A. Espinós, A. Lapuebla-Ferri, V. Albero, A. Hospitaler, Recent developments and fire design provisions for CFST columns and slim-floor beams, *J. Constr. Steel Res.* 172 (2020), 106159.
- [3] A. Espinos, L. Gardner, M.L. Romero, A. Hospitaler, Fire behaviour of concrete filled elliptical steel columns, *Thin-Walled Struct.* 49 (2) (2011) 239–255.
- [4] V. Albero, C. Ibañez, A. Piquer, D. Hernández-Figueirido, Behaviour of slender concrete-filled dual steel tubular columns subjected to eccentric loads, *J. Constr. Steel Res.* 176 (2021), 106365.
- [5] Y.-L. Long, L. Zeng, L. Gardner, M.A. Wadee, A new model for calculating the elastic local buckling stress of steel plates in square CFST columns, *Thin-Walled Struct.* 171 (2022), 108756.
- [6] W. Li, L.-H. Han, X.-L. Zhao, Axial strength of concrete-filled double skin steel tubular (CFDST) columns with preload on steel tubes, *Thin-Walled Struct.* 56 (2012) 9–20.
- [7] R. Deng, X.-H. Zhou, Y.-H. Wang, K. Ke, J.-L. Bai, R.-H. Zhu, Behaviour of tapered CFDST columns with large hollow ratio under combined loads, *J. Constr. Steel Res.* 196 (2022), 107388.
- [8] P. Montague, A simple composite construction for cylindrical shells subjected to external pressure, *J. Mech. Eng. Sci.* 17 (2) (1975) 105–113.
- [9] S. Wei, S. Mau, C. Vipulanandan, S. Mantrala, Performance of new sandwich tube under axial loading: experiment, *J. Struct. Eng.* 121 (12) (1995) 1806–1814.
- [10] K. Nakanishi, T. Kitada, H. Nakai, Experimental study on ultimate strength and ductility of concrete filled steel columns under strong earthquake, *J. Constr. Steel Res.* 51 (3) (1999) 297–319.
- [11] X.-L. Zhao, L.-H. Han, Double skin composite construction, *Prog. Struct. Eng. Mater.* 8 (3) (2006) 93–102.
- [12] F. Wang, B. Young, L. Gardner, Compressive testing and numerical modelling of concrete-filled double skin CHS with austenitic stainless steel outer tubes, *Thin-Walled Struct.* 141 (2019) 345–359.
- [13] F. Zhou, W. Xu, Cyclic loading tests on concrete-filled double-skin (SHS outer and CHS inner) stainless steel tubular beam-columns, *Eng. Struct.* 127 (2016) 304–318.
- [14] L. Gardner, Stability and design of stainless steel structures – review and outlook, *Thin-Walled Struct.* 141 (2019) 208–216.
- [15] L.-H. Han, Q.-X. Ren, W. Li, Tests on stub stainless steel–concrete–carbon steel double-skin tubular (DST) columns, *J. Constr. Steel Res.* 67 (3) (2011) 437–452.
- [16] M.F. Hassanein, O.F. Kharoob, Q.Q. Liang, Circular concrete-filled double skin tubular short columns with external stainless steel tubes under axial compression, *Thin-Walled Struct.* 73 (2013) 252–263.
- [17] F. Wang, B. Young, L. Gardner, Compressive behaviour and design of CFDST cross-sections with stainless steel outer tubes, *J. Constr. Steel Res.* 170 (2020), 105942.
- [18] F. Wang, B. Young, L. Gardner, CFDST sections with square stainless steel outer tubes under axial compression: experimental investigation, numerical modelling and design, *Eng. Struct.* 207 (2020), 110189.
- [19] F. Wang, B. Young, L. Gardner, Experimental study of square and rectangular CFDST sections with stainless steel outer tubes under axial compression, *J. Struct. Eng.* 145 (11) (2019), 04019139.
- [20] F.-C. Wang, L.-H. Han, W. Li, Analytical behavior of CFDST stub columns with external stainless steel tubes under axial compression, *Thin-Walled Struct.* 127 (2018) 756–768.
- [21] Y. Zheng, C. He, L. Zheng, Experimental and numerical investigation of circular double-tube concrete-filled stainless steel tubular columns under cyclic loading, *Thin-Walled Struct.* 132 (2018) 151–166.
- [22] H. Zhao, R. Wang, D. Lam, C.-C. Hou, R. Zhang, Behaviours of circular CFDST with stainless steel external tube: slender columns and beams, *Thin-Walled Struct.* 158 (2021), 107172.
- [23] L. Gardner, D.A. Nethercot, Stainless steel structural design: a new approach, *Struct. Eng.* 82 (21) (2004) 21–28.
- [24] Y.K.R. Gunawardena, F. Aslani, B. Uy, W.-H. Kang, S. Hicks, Review of strength behaviour of circular concrete filled steel tubes under monotonic pure bending, *J. Constr. Steel Res.* 158 (2019) 460–474.
- [25] K. Uenaka, H. Kitoh, K. Sonoda, Concrete filled double skin tubular members subjected to bending, *Steel Compos. Struct.* 8 (4) (2008) 297–312.
- [26] M.-X. Xiong, D.-X. Xiong, J.Y.R. Liew, Flexural performance of concrete filled tubes with high tensile steel and ultra-high strength concrete, *J. Constr. Steel Res.* 132 (2017) 191–202.
- [27] S.-S. Eom, Q.-V. Vu, J.-H. Choi, H.-H. Park, S.-E. Kim, Flexural behavior of concrete-filled double skin steel tubes with a joint, *J. Constr. Steel Res.* 155 (2019) 260–272.
- [28] V.Q. Vieta, H. Hab, P.T. Hoang, Evaluation of ultimate bending moment of circular concrete-filled double skin steel tubes using finite element analysis, *J. Sci. Technol. Civ. Eng. (STCE)-NUCE* 13 (1) (2019) 21–32.
- [29] X.-L. Zhao, R. Grzebieta, Strength and ductility of concrete filled double skin (SHS inner and SHS outer) tubes, *Thin-Walled Struct.* 40 (2) (2002) 199–213.
- [30] Z. Tao, L.-H. Han, Behaviour of concrete-filled double skin rectangular steel tubular beam-columns, *J. Constr. Steel Res.* 62 (7) (2006) 631–646.
- [31] J. Chen, J. Wang, F. Xie, W.-L. Jin, Behavior of thin-walled dodecagonal section double skin concrete-filled steel tubes under bending, *Thin-Walled Struct.* 98 (2016) 293–300.
- [32] L.-H. Han, Z. Tao, H. Huang, X.-L. Zhao, Concrete-filled double skin (SHS outer and CHS inner) steel tubular beam-columns, *Thin-Walled Struct.* 42 (9) (2004) 1329–1355.
- [33] Y.-F. Yang, G.-L. Ma, Experimental behaviour of recycled aggregate concrete filled stainless steel tube stub columns and beams, *Thin-Walled Struct.* 66 (2013) 62–75.
- [34] Y. Deng, B. Young, Tests on concrete-filled lean duplex stainless steel tubular members subjected to bending, in: *Proceedings of the 8th International Conference on Advances in Steel Structures*, 2015.
- [35] Y. Chen, R. Feng, L. Wang, Flexural behaviour of concrete-filled stainless steel SHS and RHS tubes, *Eng. Struct.* 134 (2017) 159–171.
- [36] Y. Chen, K. Wang, R. Feng, K. He, L. Wang, Flexural behaviour of concrete-filled stainless steel CHS subjected to static loading, *J. Constr. Steel Res.* 139 (2017) 30–43.
- [37] Y. Gunawardena, F. Aslani, Static flexural behaviour of concrete-filled spiral-welded stainless-steel tubes, *Thin-Walled Struct.* 151 (2020), 106731.
- [38] Y. Gunawardena, F. Aslani, Finite element modelling of concrete-filled spiral-welded mild-steel and stainless-steel tubes in flexure, *Structures* 32 (2021) 792–816.
- [39] F. Wang, B. Young, L. Gardner, Testing and numerical modelling of circular CFDST cross-sections with stainless steel outer tubes in bending, *Eng. Struct.* 247 (2021), 113170.
- [40] EN 1994-1-1, Eurocode 4: design of composite steel and concrete structures, in: *Part 1.1: General Rules and Rules for Buildings*, European Committee for Standardization (CEN), Brussels, 2004.
- [41] AISC 360, Specification for Structural Steel Buildings, American Institute of Steel Construction, Chicago, USA, 2016.
- [42] L. Gardner, X. Yun, Description of stress-strain curves for cold-formed steels, *Constr. Build. Mater.* 189 (2018) 527–538.
- [43] F. Wang, Y. Liang, O. Zhao, B. Young, Pin-ended press-braked S960 ultra-high strength steel angle section columns: testing, numerical modelling and design, *Eng. Struct.* 228 (2021), 111418.
- [44] ACI 318, Building Code Requirements for Structural Concrete and Commentary. Michigan, USA, Farmington Hills, 2014.
- [45] F. Wang, O. Zhao, B. Young, Flexural behaviour and strengths of press-braked S960 ultra-high strength steel channel section beams, *Eng. Struct.* 200 (2019), 109735.
- [46] J. Chen, T.-M. Chan, Experimental assessment of the flexural behaviour of concrete-filled steel tubular beams with octagonal sections, *Eng. Struct.* 199 (2019), 109604.
- [47] G.B. dos Santos, L. Gardner, M. Kucukler, A method for the numerical derivation of plastic collapse loads, *Thin-Walled Struct.* 124 (2018) 258–277.
- [48] ABAQUS, ABAQUS/standard user's manual, in: Version 6.17. Dassault Systemes Simulia Corp. USA, 2017.
- [49] B. Mou, X. Liu, F. Wang, H. Xiao, Cyclic testing on prefabricated joints for steel beam to concrete-filled steel tubular column, *J. Constr. Steel Res.* 194 (2022), 107345.
- [50] A. He, F. Wang, O. Zhao, Experimental and numerical studies of concrete-filled high-chromium stainless steel tube (CFHSST) stub columns, *Thin-Walled Struct.* 144 (2019), 106273.
- [51] D.S. Castanheira, L.R.O. de Lima, P.C.G. da S Vellasco, K.A. Cashell, L. Gardner, Compressive behaviour of double skin sections with stainless steel outer tubes and recycled aggregate concrete, *Structures* 41 (2022) 750–763.
- [52] Z. Tao, Z.B. Wang, Q. Yu, Finite element modelling of concrete-filled steel stub columns under axial compression, *J. Constr. Steel Res.* 89 (2013) 121–131.
- [53] M. Cabrera, W. Tizani, J. Ninic, F. Wang, Experimental and numerical analysis of preload in extended hollow-bolt blind bolts, *J. Constr. Steel Res.* 186 (2021), 106885.
- [54] I. Arrayago, E. Real, E. Mirambell, L. Gardner, The continuous strength method for the design of stainless steel hollow section columns, *Thin-Walled Struct.* 154 (2020), 106825.
- [55] M. Theofanous, T.M. Chan, L. Gardner, Flexural behaviour of stainless steel oval hollow sections, *Thin-Walled Struct.* 47 (6–7) (2009) 776–787.
- [56] L. Gardner, X. Yun, F. Walport, The continuous strength method – review and outlook, *Eng. Struct.* 275 (2023), 114924.
- [57] J.Y.R. Liew, M.-X. Xiong, D.-X. Xiong, Design of concrete filled tubular beam-columns with high strength steel and concrete, *Structures* 8 (2016) 213–226.
- [58] EN 1990:2002, Eurocode — Basis of Structural Design, European Committee for Standardization (CEN), Brussels, 2002.